# Quantum paramagnetism in the decorated square-kagome antiferromagnet $Na_6Cu_7BiO_4(PO_4)_4Cl_3$ – Supplemental Material –

Nils Niggemann,[1,2,3,*] Nikita Astrakhantsev,[4,*] Arnaud Ralko,[5,3,*] Francesco Ferrari,[6,3,*] Atanu Maity,[3] Tobias Müller,[7] Johannes Richter,[8,9] Ronny Thomale,[7,3] Titus Neupert,[4] Johannes Reuther,[1,2,3] Yasir Iqbal,[3] and Harald O. Jeschke[10,3]

[1]*Dahlem Center for Complex Quantum Systems and Fachbereich Physik, Freie Universität Berlin, 14195 Berlin, Germany*
[2]*Helmholtz-Zentrum für Materialien und Energie, Hahn-Meitner-Platz 1, 14109 Berlin, Germany*
[3]*Department of Physics and Quantum Centre of Excellence for Diamond and Emergent Materials (QuCenDiEM), Indian Institute of Technology Madras, Chennai 600036, India*
[4]*Department of Physics, University of Zürich, Winterthurerstrasse 190, CH-8057 Zürich, Switzerland*
[5]*Institut Néel, UPR2940, Université Grenoble Alpes, CNRS, Grenoble, FR-38042 France*
[6]*Institut für Theoretische Physik, Goethe Universität Frankfurt, Max-von-Laue-Straße 1, 60438 Frankfurt am Main, Germany*
[7]*Institut für Theoretische Physik und Astrophysik, Julius-Maximilians-Universität Würzburg, Am Hubland, D-97074 Würzburg, Germany*
[8]*Institut für Physik, Otto-von-Guericke-Universität Magdeburg, P.O. Box 4120, 39016 Magdeburg, Germany*
[9]*Max-Planck-Institut für Physik Komplexer Systeme, Nöthnitzer Straße 38, D-01187 Dresden, Germany*
[10]*Research Institute for Interdisciplinary Science, Okayama University, Okayama 700-8530, Japan*

(Dated: December 12, 2023)

## ADDITIONAL DFT INFORMATION

Density functional theory calculations were performed with the full potential local orbital (FPLO) basis [S2] and a generalized gradient approximation (GGA) exchange correlation functional [S3]. Strong electronic correlations on Cu $3d$ orbitals are taken into account by a DFT+U method [S4]. We show the full result of the energy mapping procedure for $Na_6Cu_7BiO_4(PO_4)_4Cl_3$ in Table S1. For every considered value of the onsite interaction strength $U$, a total of 68 energies were calculated with $4\times4\times4$ **k**-point meshes. The line in bold face is interpolated to yield the experimental Curie-Weiss temperature $\theta_{\mathrm{CW}} = -212\,\mathrm{K}$ [S1]. As discussed in the main text, only five of the thirteen determined exchange interactions are substantial and are considered in the many-body calculations for $Na_6Cu_7BiO_4(PO_4)_4Cl_3$. The only interlayer coupling $J_{15}$ we determined is small enough that $Na_6Cu_7BiO_4(PO_4)_4Cl_3$ can be treated as a 2D system.

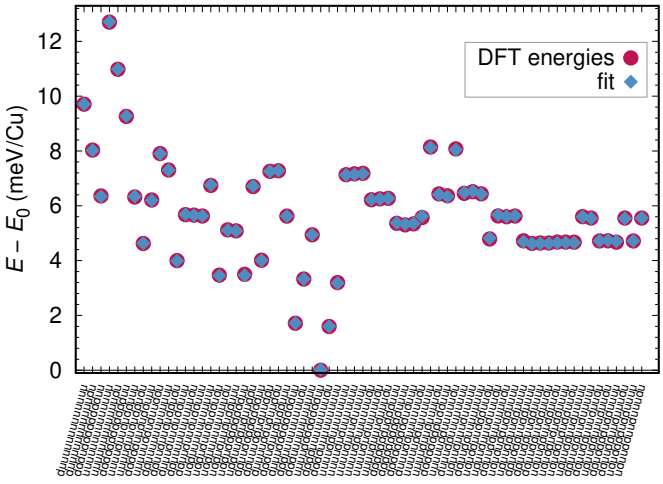


FIG. S1. Quality of energy mapping in $Na_6Cu_7BiO_4(PO_4)_4Cl_3$. 68 calculated DFT energies are very precisely matched by the Heisenberg Hamiltonian with 13 exchange interactions.

In Fig. S1, we show that the energy mapping approach works very well for $Na_6Cu_7BiO_4(PO_4)_4Cl_3$. In $P1$ symmetry, all 14 $Cu^{2+}$ moments can be set independently, and for the 68 chosen spin configurations, the comparison between DFT energy and fit to the Heisenberg Hamiltonian is excellent.

## LATTICE CONVENTION

Each layer of the compound $Na_6Cu_7BiO_4(PO_4)_4Cl_3$ is represented by a square-kagome lattice with an additional site at the center of each shuriken (square surrounded by four triangles). More precisely, we define the unit vectors

$$\mathbf{a}_1 = (1,0), \quad \mathbf{a}_2 = (0,1), \tag{S1}$$

and a unit cell consisting of seven sites, labelled from $A$ to $G$ as shown in Fig. S2, whose relative coordinates are

$$\begin{aligned} &\boldsymbol{\delta}_A = (0,1/2),\ \boldsymbol{\delta}_B = (1/4,3/4) \\ &\boldsymbol{\delta}_C = (1/4,1/4),\ \boldsymbol{\delta}_D = (3/4,1/4) \\ &\boldsymbol{\delta}_E = (3/4,3/4),\ \boldsymbol{\delta}_F = (1/2,1) \\ &\boldsymbol{\delta}_G = (2/4,2/4) \end{aligned} \tag{S2}$$

In this convention, all sites lie at rational fractions of the basis vectors, which ensures a finite extended Brillouin zone over which the structure factor is periodic. The lattice for this compound features three types of symmetry inequivalent sites, namely those that lie on the vertices of each shuriken $(A, F)$, the corners of each square $(B, C, D, E)$ and the center sites $G$ [see Fig. S2]. Although, the geometry of the lattice does not alter the physics (once the couplings are fixed), for comparison with experiments, it is required to compute Fourier-transformed quantities with respect to the lattice of the original compound. As most numerical methods do not explicitly employ real-space crystallographic coordinates but

| $U$ (eV) | $J_1$ (K) | $J_2$ (K) | $J_3$ (K) | $J_4$ (K) | $J_5$ (K) | $J_6$ (K) | $J_8$ (K) | $J_9$ (K) | $J_{10}$ (K) | $J_{13}$ (K) | $J_{14}$ (K) | $J_{15}$ (K) | $J_{20}$ (K) | $\theta_{\mathrm{CW}}$ (K) |
|---|---|---|---|---|---|---|---|---|---|---|---|---|---|---|
| 6.5 | 113.6(8) | 191.5(7) | 158.7(1.4) | 48.1(4) | 5.8(4) | 0.6(4) | -0.8(7) | 3.4(8) | 66.6(2) | -2.2(6) | 2.0(4) | 0.3(4) | -0.1(4) | -218.7 |
| **6.66** | **109.1(8)** | **186.2(7)** | **155.3(1.4)** | **46.9(4)** | **5.3(4)** | **0.6(4)** | **-1.1(7)** | **3.2(8)** | **64.6(2)** | **-2.2(6)** | **1.9(4)** | **0.3(4)** | **0.0(4)** | **-212** |
| 7 | 100.1(7) | 175.5(6) | 148.1(1.1) | 44.6(4) | 4.4(4) | 0.5(3) | -1.5(5) | 2.9(7) | 60.5(2) | -2.1(5) | 1.8(3) | 0.2(4) | 0.0(3) | -198.6 |
| 7.5 | 88.2(6) | 160.8(5) | 137.8(9) | 41.3(3) | 3.2(3) | 0.5(3) | -1.9(4) | 2.6(6) | 54.9(2) | -2.1(4) | 1.6(3) | 0.2(3) | 0.0(2) | -180.5 |
| 8 | 77.7(5) | 147.3(4) | 128.0(7) | 38.2(2) | 2.3(3) | 0.4(2) | -2.2(4) | 2.2(5) | 49.8(1) | -2.0(3) | 1.5(2) | 0.2(2) | 0.0(2) | -164.1 |
| 8.5 | 68.3(4) | 134.8(3) | 118.6(6) | 35.3(2) | 1.6(2) | 0.4(2) | -2.4(3) | 2.0(4) | 45.3(1) | -1.8(3) | 1.4(2) | 0.1(2) | 0.0(2) | -149.1 |
| $d$ (Å) | 3.11405 | 3.27801 | 4.40394 | 5.0088 | 5.26566 | 5.33981 | 5.72746 | 5.76923 | 6.01815 | 6.55602 | 7.08351 | 7.71676 | 8.22822 | |

TABLE S1. Exchange interactions of $Na_6Cu_7BiO_4(PO_4)_4Cl_3$ obtained by DFT energy mapping as described in the main text. The line in bold face corresponds to the set of couplings that match the experimental Curie-Weiss temperature [S1].

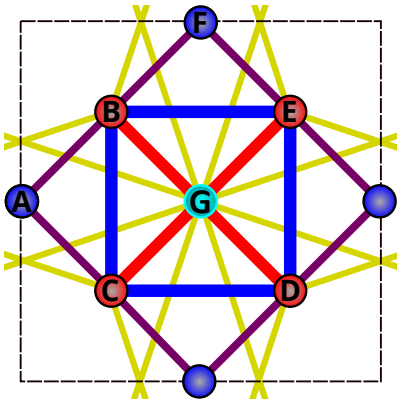


FIG. S2. Idealized square-kagome unit cell. Sites A and F correspond to Cu(1) ions, sites B, C, D, E to Cu(2) ions and site G to the Cu(3) ion in the unit cell of $Na_6Cu_7BiO_4(PO_4)_4Cl_3$.

rather the more abstract graph of sites and respective bonds, this amounts to a choice in the post-processing of real-space data. In the following, we outline this step in detail. We define the Fourier transform of the spin susceptibility as

$$\chi(\mathbf{q}) = \frac{1}{N}\sum_{i,j}\chi(\mathbf{r}_i,\mathbf{r}_j)e^{i\mathbf{q}\cdot(\mathbf{r}_i-\mathbf{r}_j)}. \tag{S3}$$

Here, the vectors $\mathbf{q}, \mathbf{r}_i$ are three-dimensional, accounting for the true crystallographic coordinates, and allowing for distortions outside of the square-kagome planes which occur in the crystal structure. We must therefore map each pair of sites of the true 3D lattice to a unique site in the idealized lattice.

Upon noting that the layers are decoupled (as we neglect the tiny $J_{15}$ exchange interaction) and correlations between two sites from different layers are zero, we can immediately interpret the summation to go over sites in a single layer only.

The mapping we need to perform can then be written as $f(n_1, n_2, 0, n_b) = (n_1', n_2', n_b')$, where we define $\mathbf{r}_i = n_1\mathbf{a}_1 + n_2\mathbf{a}_2 + \mathbf{b}_{n_b}$. Since the unit cell of the three-dimensional lattice can be enlarged compared to the idealized one, it may be cumbersome to find this mapping directly. A convenient strategy is to work in Cartesian coordinates, mapping $\mathbf{r}_i$ to a $2D$ point $(x, y)$ which lies on the idealized lattice. Then, the Cartesian coordinates $(x, y)$ can be transformed back into either a lattice position $(n_1, n_2, n_b)$, or a site index $i$. This is shown in Fig. S3.

To compare with powder samples, we compute the powder

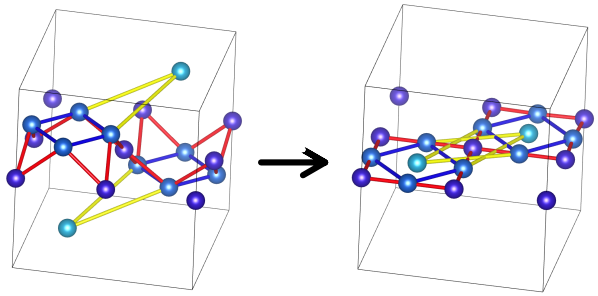

FIG. S3. Mapping from 3D lattice to 2D lattice. To compute Eq. (S3), sites are mapped to the idealized lattice convention. Visualization done using VESTA [S5].

averaged structure factor

$$S(Q) \equiv \frac{1}{4\pi}\int d\Omega S(\mathbf{q}), \quad Q = |\mathbf{q}| \tag{S4}$$

and multiply by the form factor to account for nuclear scattering on $Cu^{2+}$ ions [S6]

$$\begin{aligned} f(Q) &= Ae^{-a\frac{Q^2}{4\pi}} + Be^{-b\frac{Q^2}{4\pi}} + C_1e^{-c\frac{Q^2}{4\pi}} + D_1 \qquad \text{(S5)}\\ A &= 0.0232,\ B = 0.4023\\ C_1 &= 0.5882,\ D_1 = -0.0137\\ a &= 34.969,\ b = 11.564,\ c = 3.843. \end{aligned}$$

## METHODS

### Many-variable variational Monte Carlo (mVMC)

In this work, we employ the many-variable variational Monte Carlo implementation presented in Refs. [S7, S8]. To apply mVMC, spin operators are first mapped to pseudo-fermionic bilinears through the Abrikosov representation

$$\hat{\mathbf{S}}_i = \frac{1}{2}\sum_{\alpha,\beta=\downarrow,\uparrow}\hat{c}^\dagger_{i,\alpha}\boldsymbol{\sigma}_{\alpha,\beta}\hat{c}_{i,\beta}\,. \tag{S6}$$

Inspired by Anderson's resonating valence-bond wave function, the mVMC ansatz has the form

$$|\phi_{\mathrm{pair}}\rangle = \hat{\mathcal{P}}^{\infty}_{\mathrm{G}}\exp\left(\sum_{i,j}f_{i,j}\hat{c}^\dagger_{i,\uparrow}\hat{c}^\dagger_{j\downarrow}\right)|0\rangle, \tag{S7}$$

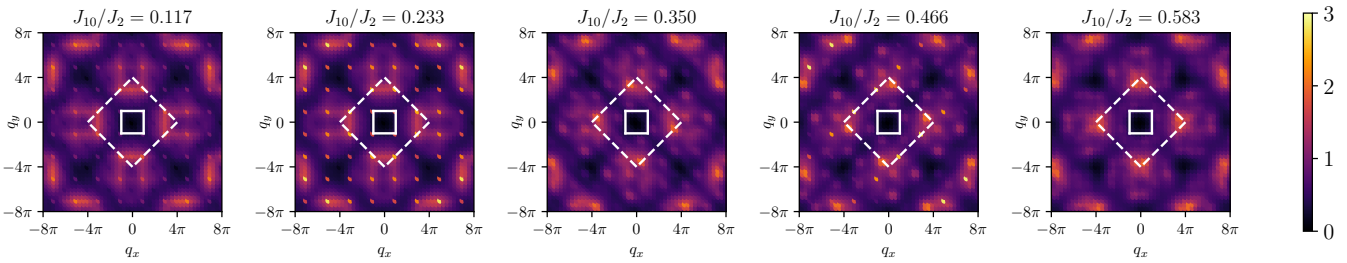


FIG. S4. Momentum-resolved equal-time spin structure factor calculated from mVMC on the $6 \times 6 \times 6$ lattice for different values of $J_{10}/J_2$. The Fourier transform is performed with respect to the ideal lattice coordinates of Eq. (S2). The wave functions were obtained with the symmetrization technique, enforcing the trivial representation. The solid and dashed lines denote the first and the extended Brillouin zones, respectively. The corresponding energies of these wave functions are given in Table S2.

where a fermionic wave function is constrained to a space of singly occupied sites by means of the Gutzwiller projector $\hat{\mathcal{P}}_{\mathrm{G}}^{\infty} = \prod_i (n_{i,\uparrow} - n_{i,\downarrow})^2$, where $n_{i,\sigma} = \hat{c}_{i,\sigma}^{\dagger}\hat{c}_{i,\sigma}$. The wave-function value $\langle \boldsymbol{\sigma} | \phi_{\mathrm{pair}} \rangle$ for a specific spin configuration $|\boldsymbol{\sigma}\rangle$ is evaluated using the Slater determinant of the matrix with elements $f_{i,j}$. The parameters $f_{i,j}$ are optimized using the stochastic reconfiguration optimization technique [S9–S11].

We may force a wave function to transform as a specific irreducible representation of the symmetry group. To this end, we apply its generators until the symmetry orbit is exhausted

$$|\Psi_\xi\rangle = \hat{P}|\Psi\rangle = \sum_n \xi^n \hat{G}^n |\Psi\rangle, \tag{S8}$$

where $\xi$ is the desired projection quantum number and $|\Psi_\xi\rangle$ the resulting symmetrized state. In the `mVMC` package, the projection onto the total spin $S$ is performed by superposing the $SU(2)$–rotated wave functions [S8].

In Fig. S4, we show the equal-time spin structure factor for different values of $J_{10}/J_2$ measured within mVMC on the $6 \times 6$ lattice. The corresponding wave function energies are given in Table S2. One may see that the frustration grows until $J_{10}/J_2 \approx 0.3$, which is manifested by growing energy and progressively diffuse character of the structure factor, and then rapidly decays with further increase in $J_{10}/J_2$.

### Variational Monte Carlo (VMC)

Analogously to mVMC, the fermionic variational Monte Carlo calculations of this work make use of a Gutzwiller-projected wave function to approximate the ground state of the spin Hamiltonian by minimization of the variational energy. The VMC trial state reads

$$|\Psi_0\rangle = \hat{\mathcal{J}}\hat{\mathcal{P}}_{\mathrm{G}}^{\infty}|\Phi_0\rangle, \tag{S9}$$

| $J_{10}/J_2$ | 0.0 | 0.117 | 0.223 | 0.350 | 0.466 | 0.583 |
|---|---|---|---|---|---|---|
| $E/J_2$ | $-0.4128$ | $-0.4128$ | $-0.4080$ | $-0.4305$ | $-0.4436$ | $-0.4687$ |

TABLE S2. Ground state energy $E/J_2$ per site obtained on the $6 \times 6$ lattice within mVMC for different ratios of $J_{10}/J_2$. The statistical error is kept around $\delta E/J_2 = 10^{-4}$.

where $\hat{\mathcal{P}}_{\mathrm{G}}^{\infty}$ is the Gutzwiller projector, $|\Phi_0\rangle$ is a fermionic Slater determinant [in the Abrikosov fermion representation of spins Eq. (S6)] and $\hat{\mathcal{J}}$ is a spin-spin Jastrow factor. The definition of the fermionic state $|\Phi_0\rangle$ is done by the introduction of an auxiliary fermionic Hamiltonian

$$\hat{\mathcal{H}}_0 = \sum_{i,j,\alpha} \chi_{ij} \hat{c}_{i,\alpha}^{\dagger} \hat{c}_{j,\alpha}, \tag{S10}$$

whose hopping amplitudes, $\chi_{ij}$, play the role of variational parameters. The presence of the spin-spin Jastrow factor

$$\hat{\mathcal{J}} = \exp\left(\sum_{i,j} v_{i,j} \hat{S}_i^z \hat{S}_j^z\right) \tag{S11}$$

can enhance/suppress spin-spin correlations between lattice sites. We consider a long-range Jastrow factor with pseudopotential parameters that depend on the distance between sites, i.e., $v_{i,j} = v(\|\mathbf{r}_i - \mathbf{r}_j\|)$. The variational parameters defining $|\Psi_0\rangle$ are optimized by means of the stochastic reconfiguration method [S9, S10]. The VMC calculations are performed on finite-size lattices with periodic boundary conditions. Specifically, we employ two kinds of fully-symmetric clusters, one defined by the translation vectors $\mathbf{T}_1 = L\mathbf{a}_1$ and $\mathbf{T}_2 = L\mathbf{a}_2$ (containing $N_s = 7L^2$ sites), and the other defined by the vectors $\mathbf{T}_1 = L(\mathbf{a}_1 + \mathbf{a}_2)$ and $\mathbf{T}_2 = L(\mathbf{a}_1 - \mathbf{a}_2)$ (containing $N_s = 14L^2$ sites). The biggest lattice employed in our VMC calculations contains $N_s = 700$ spins.

The best variational energy is obtained by a parametrization of the auxiliary Hamiltonian in which the translational symmetry is broken. In particular, in agreement with mVMC observations, the optimal hopping pattern requires a doubling of the unit cell along $\mathbf{a}_1$ and $\mathbf{a}_2$ ($2 \times 2$ periodicity). Concerning point group symmetries, the VMC wave function turns out to preserve the $C_4$ rotational symmetry around the center of the $2 \times 2$ supercell. The small $C_4$ to $C_2$ symmetry breaking found by mVMC calculations is not captured by the VMC variational ansatz. The spin structure factor $S(\mathbf{q})$ corresponding to the best variational state for the Heisenberg Hamiltonian of $Na_6Cu_7BiO_4(PO_4)_4Cl_3$ is shown in Fig. S5. The absolute maxima of $S(\mathbf{q})$ are located at $\mathbf{q} = (7\pi/2, \pi/2)$ and $\mathbf{q} = (\pi/2, 7\pi/2)$ (and symmetry related points). Compared

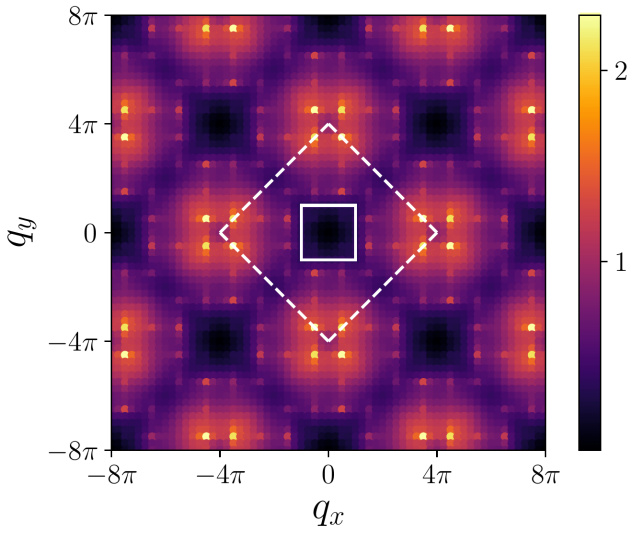


FIG. S5. Equal-time spin structure factor $S(\mathbf{q})$ from VMC for the Hamiltonian of $Na_6Cu_7BiO_4(PO_4)_4Cl_3$. The results are obtained on a cluster with $N_s = 448$ sites, defined by the translation vectors $\mathbf{T}_1 = 8\mathbf{a}_1$ and $\mathbf{T}_2 = 8\mathbf{a}_2$, and plotted within the reciprocal space of the idealized lattice. The solid and dashed lines denote the first and the extended Brillouin zones, respectively.

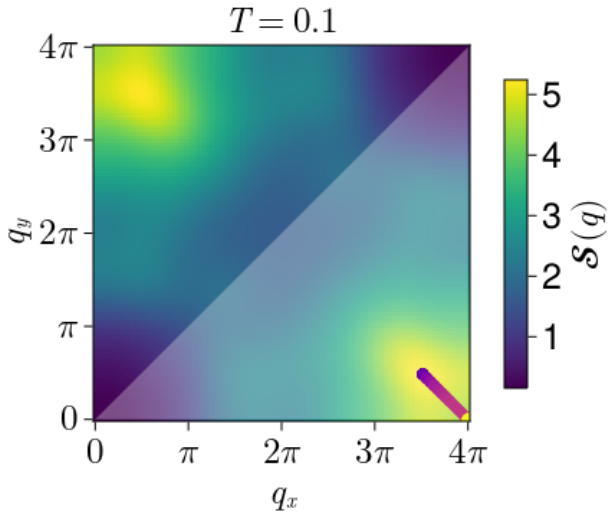


FIG. S6. Evolution of the maxima of the equal-time spin structure factor as a function of temperature obtained from PMFRG. The color of the line corresponds to the temperature, i.e., the yellow part corresponds to the highest simulated temperature ($T = 2.5J_2$, while the blue part indicates the lowest temperatures. The background shows the low temperature structure factor as a reference.

to mVMC results, we find a larger intensity of the peaks of the structure factor, which can be ascribed to the presence of the Jastrow factor that enhances antiferromagnetic correlations.

## PMFRG

The PMFRG formalism expresses spin operators by three different flavors $(x, y, z)$ of Majorana fermions

$$S_i^x = -i\eta_i^y\eta_i^z, \qquad S_i^y = -i\eta_i^z\eta_i^x, \qquad S_i^z = -i\eta_i^x\eta_i^y. \tag{S12}$$

This representation has the advantage that no unphysical states are introduced, allowing for quantitatively correct predictions at finite temperature [S12, S13]. One of the key advantages of PMFRG is its high momentum space resolution which allows for an easy detection of incommensurate order. The only restriction is a cut-off of all correlations beyond a numerically chosen maximum distance $L$. In a paramagnet, correlation lengths are typically small and effectively zero beyond a characteristic correlation length $\xi$, which makes this approximation virtually exact. When the correlation length diverges, for instance at the critical point of a phase transition, a finite-size scaling analysis may be performed to give accurate estimates of the critical temperature [S13].

Figure S6 shows the equal-time spin structure factor at low temperature, featuring soft maxima at wave-vectors $(q_x, q_y) \sim (3\pi, \pi/2)$. We find the position of these maxima to be temperature dependent. At high temperatures $T \gg J_2$, the maxima reside at $(4\pi, \pi)$ and symmetry related points, while the position of the peak shifts as temperature is lowered. In addition to the spin susceptibility $\chi$ defined in Eq. (S3), one may also define a sublattice-resolved susceptibility $\chi_{\alpha\beta}$, $\alpha, \beta = 1, 2, \ldots N_{\text{UC}}$, where $N_{\text{UC}} = 7$ such that $\chi(\mathbf{k}) = \frac{1}{N_{\text{UC}}}\sum_{\alpha\beta}\chi_{\alpha\beta}(\mathbf{k})$. To study the influence of the

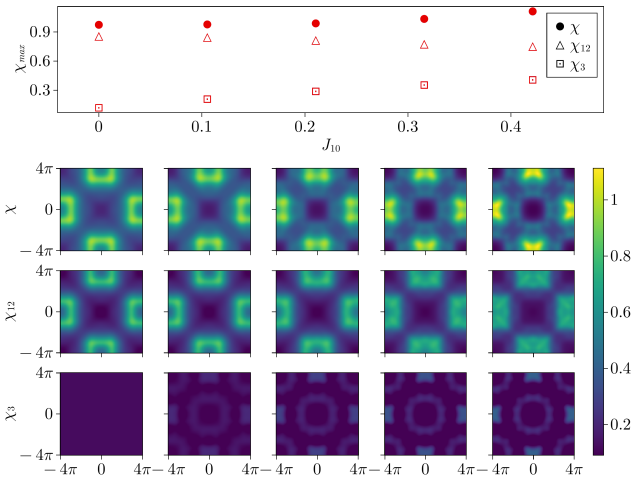


FIG. S7. From PMFRG, we show the evolution of the sublattice dependent susceptibilities defined in Eq. (S13) as a function of $J_{10}$. The top panel shows the respective maxima in momentum space, while the heat maps show the full momentum dependence. Note that points are shown for three different maximal correlation lengths of $L = 14, 16, 18$ nearest neighbor bonds, which all coincide, indicating absence of finite size effects.

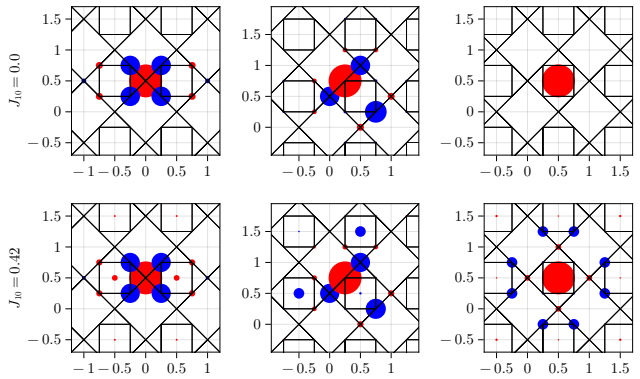


FIG. S8. Real space correlations $\langle \hat{\mathbf{S}}_i \cdot \hat{\mathbf{S}}_j \rangle$ computed from PMFRG by taking Cu(1) (left), Cu(2) (middle), and Cu(3) (right) as reference sites $i$. The radii of the circle indicates the strength of correlations, while the color red (blue) indicates a positive (negative) sign of the correlations.

Cu(3) sites, Fig. S7 further displays the susceptibilities

$$\chi_{12}(\mathbf{k}) \equiv \frac{1}{N_{\mathrm{UC}}} \sum_{\alpha\beta \neq Cu(3)} \chi_{\alpha\beta}(\mathbf{k})$$
$$\chi_3(\mathbf{k}) \equiv \chi(\mathbf{k}) - \chi_{12}(\mathbf{k}). \tag{S13}$$

Here, $\chi_{12}$ quantifies the correlations between all non-Cu(3) sites, and $\chi_3$ the contribution to the susceptibility upon adding the Cu(3) site. The correlations between the Cu(1) and Cu(2) sites decrease upon strengthening the $J_{10}$ bond while maxima of intensity become diffuse, indicating increased frustration. To see this, note that the conservation of spin magnitude dictates a sum rule within the extended BZ: $\sum_i \hat{\mathbf{S}}_i^2 = \sum_{\mathbf{q}} \langle \hat{\mathbf{S}}(-\mathbf{q}) \hat{\mathbf{S}}(\mathbf{q}) \rangle = \mathrm{N}\frac{3}{4}$. As a consequence, the susceptibility $\chi_{\alpha\beta}(\mathbf{q})$ for non-interacting spins must be a non-zero constant (see, e.g., $\chi_3$ in Fig. S7 at $J_{10} = 0$). Switching on the couplings between sites, leaves the sum rule intact for each sublattice but intensities may shift in reciprocal space and develop features. Therefore, the observed decrease in the maximum of $\chi_{12}$ indicates a more uniform distribution of different ordering wavevectors $\mathbf{q}$ within the system –a signature of the effects of frustration.

While the correlations between Cu(3) sites and the rest of the system naturally grow as they are increasingly coupled, ordering tendencies are absent as visible from the independence of our data on the maximal correlation length $L$ above the accessible temperature range of $T \gtrsim 0.3 J_2$.

In Fig. S8, we also show the pattern of equal time spin-spin correlations in real space for the system with $J_{10} = 0$ and $J_{10} \approx 0.42 J_2$. It is visible that adding the additional Cu(3) site does not lead to increased correlations between the other sites and, in fact, slightly decreases them. Overall, we find good agreement to mVMC in Fig. 2 of the main text.

For comparison with experimental data, we compute the spin structure factor with respect to the actual crystal lattice site coordinates, i.e., allowing for atoms to be positioned out-

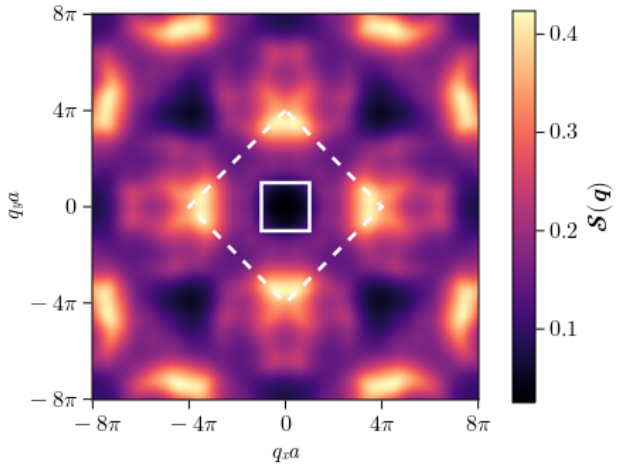


FIG. S9. Equal time structure factor $S(q, t = 0)$ at $T = 0.3 J_2$ for a cut at $q_z = 0$ computed with respect to the true, three dimensional crystallographic unit cell. Shown is the first BZ (solid), and the approximate extended BZ (dashed).

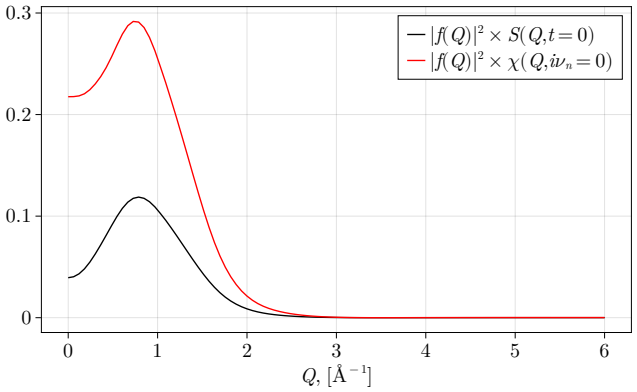


FIG. S10. Powder average of the equal time structure factor $S(Q, t = 0)$ and the static magnetic suscepibility $\chi(Q, i\nu_n = 0)$ at $T = 0.1 J_2$ obtainde from PMFRG. As in Fig. S9, the Fourier transform is performed with respect to the actual crystal lattice site coordinates.

side of a pure 2D layer. Figure S9 shows the corresponding momentum resolved equal-time spin structure factor projected onto the $q_x - q_y$ plane taking $q_z = 0$. We note that due to the irrational coordinates of the atoms within the unit cell, the structure factor is no longer periodic within any extended Brillouin zone. The structure factor permits points of high intensity away from $q_z = 0$, although they will naturally be broad, as length of correlations is limited in $z$ direction due to the layered structure of the material. If we restrict ourselves to a finite box in momentum space between $|q_{x,y,z}| < 8\pi/a$, the maxima are positioned at incommensurate positions $\mathbf{k} = (0.61, 6.95, 0)\, \pi/a$. For experimental com-

parison, in Fig. S10, we further provide the powder averaged structure factor Eq. (S4).

## SCHWINGER BOSON MEAN FIELD THEORY

As in the VMC section, it is possible to make a parton construction of the spin by introducing Schwinger bosons instead of Abrikosov fermions. We thus consider the decoupling:

$$\hat{\mathbf{S}}_i = \frac{1}{2} \sum_{\alpha,\beta=\downarrow,\uparrow} \hat{b}^\dagger_{i,\alpha} \boldsymbol{\sigma}_{\alpha,\beta} \hat{b}_{i,\beta}, \tag{S14}$$

where $\hat{b}^{(+)}$ are now bosonic operators. The advantage of dealing with bosons as opposed to fermions is the possibility of having Bose condensation and thus to easily access quantum magnetic orders as well as ($\mathbb{Z}_2$) quantum spin liquids, which are both treated on an equal footing. Here, we recall the main lines of the approach noting that more details can be found in [S14–S18]. In this approach, it is possible to write Heisenberg terms as function of two SU(2) invariant operators $\hat{A}$ and $\hat{B}$

$$\hat{A}_{ij} = \frac{1}{2}\left[\hat{b}_{i\uparrow}\hat{b}_{j\downarrow} - \hat{b}_{i\downarrow}\hat{b}_{j\uparrow}\right]$$
$$\hat{B}_{ij} = \frac{1}{2}\left[\hat{b}^+_{i\uparrow}\hat{b}_{j\uparrow} + \hat{b}^+_{i\downarrow}\hat{b}_{j\downarrow}\right]$$

as

$$\hat{\mathbf{S}}_i\hat{\mathbf{S}}_j = :\hat{B}^+_{ij}\hat{B}_{ij}: - \hat{A}^+_{ij}\hat{A}_{ij}, \tag{S15}$$

where :: denotes the normal ordering. At the mean field level, the Hamiltonian then reads

$$\mathcal{H}_{\text{SB}} = = \sum_{i,j} J_{ij}\left[\hat{B}^+_{ij}B_{ij} + \hat{B}_{ij}B^*_{ij} - \hat{A}^+_{ij}A_{ij} - \hat{A}_{ij}A^*_{ij}\right] - \sum_{i,j} J_{ij}\left[|B_{ij}|^2 - |A_{ij}|^2\right] + \sum_i \lambda_i(\hat{n}_i - 2S), \tag{S16}$$

with the mean field parameters $A_{ij} = \langle\phi_0|\hat{A}_{ij}|\phi_0\rangle$ and $B_{ij} = \langle\phi_0|\hat{B}_{ij}|\phi_0\rangle$ computed in $|\phi_0\rangle$ – the boson vacuum at $T = 0$ for each pair of interacting spins $(i \to j)$. Because the Hilbert space is enlarged by the mapping, it is necessary to fulfill the constraint $\hat{n}_i = \hat{b}^+_{i\uparrow}\hat{b}_{i\uparrow} + \hat{b}^+_{i\downarrow}\hat{b}_{i\downarrow} = 2S$ for a spin $S$. Thus, we have also introduced Lagrange multipliers $\lambda_i$ to account for this on average. Another advantage of the method is that $S$ can be treated as an external parameter and by reducing it, it is possible to enhance quantum fluctuations. This is particularly interesting if one wants to focus on phase transitions between a magnetically ordered state and its quantum spin liquid parent. Also, the flexibility of the method allows to compute the dynamical structure factor

$$S(\mathbf{q},\omega) = \frac{1}{n_s}\sum_{i,j} e^{i\mathbf{q}\cdot(\mathbf{r_i}-\mathbf{r_j})}\int_{-\infty}^{\infty} dt e^{-i\omega t}\langle\hat{\mathbf{S}}_i(t)\hat{\mathbf{S}}_j(0)\rangle, \tag{S17}$$

and to extract relevant magnon features and study Bose condensations of specific branches. Here, $n_s$ is the total number of sites given by $n_u \times 2 \times l \times l$, with $n_u$ the number of sites per unit-cell (here 14 in the presence of the Cu(3) atoms), and $l$ is the linear size of the system. This allows for comparison with neutron experiments.

In Fig. 4 of the main text, we show the dynamical structure factor for two representative spin values $S = 0.12, 0.15$ at which a quantum spin liquid (QSL) can be achieved, and for various values of Cu(3) coupling $J_{10}$ for a system size of $l = 12$ with 4032 spins, showing the proximity of the phase transition between a quantum spin liquid state and its Bose condensate counterpart.

As seen in the fermion approaches, the effect of projecting the wave function onto exact physical states increases the quantum fluctuations and helps the system to remain disordered even in the presence of the Cu(3) atoms. In the Schwinger boson mean field theory, since magnetic orders are more competitive by construction, they are favoured at $S = 1/2$. Thus, in order to reach the QSL, one has to reduce the spin value. In Fig. 4 of the main text, we can see that the Bose condensation arises on the Cu(3) spins while the others on the square-kagome lattice remains mainly disordered. This is reflected by a clear gap in the lower panels between the condensed branches and the excitations in the continuum. To have a better view of this feature, we have plotted in Fig. S11 the real-space (equal-time) spin-spin correlations using three different reference sites on a Cu(3) spin (top panel), on a corner of a triangle (middle panel) and on a corner of a square plaquette (bottom panel).

As one can see, a clear magnetic order appears on the Cu(3) spins while the ones on the remaining square-kagome lattice are disordered. This last feature is in good agreement with the observations of increased correlations between the Cu(3) sites in PMFRG, although no order could be detected in the accessible temperature regime.

---

* These authors contributed equally.


[S1] O. V. Yakubovich, L. V. Shvanskaya, G. V. Kiriukhina, A. S. Volkov, O. V. Dimitrova, and A. N. Vasiliev, Hydrothermal Synthesis and a Composite Crystal Structure of $Na_6Cu_7BiO_4(PO_4)_4[Cl,(OH)]_3$ as a Candidate for Quantum Spin Liquid, Inorg. Chem. **60**, 11450 (2021).

[S2] K. Koepernik and H. Eschrig, Full-potential nonorthogonal local-orbital minimum-basis band-structure scheme, Phys. Rev. B **59**, 1743 (1999).

[S3] J. P. Perdew, K. Burke, and M. Ernzerhof, Generalized gradient approximation made simple, Phys. Rev. Lett. **77**, 3865 (1996).

[S4] A. I. Liechtenstein, V. I. Anisimov, and J. Zaanen, Density-functional theory and strong interactions: Orbital ordering in Mott-Hubbard insulators, Phys. Rev. B **52**, R5467 (1995).

[S5] K. Momma and F. Izumi, *VESTA3* for three-dimensional visualization of crystal, volumetric and morphology data, J. Appl. Crystallogr. **44**, 1272 (2011).

[S6] P. Ghosh, T. Müller, Y. Iqbal, R. Thomale, and H. O. Jeschke, Effective spin-1 breathing kagome Hamiltonian induced by the exchange hierarchy in the maple leaf mineral bluebellite,

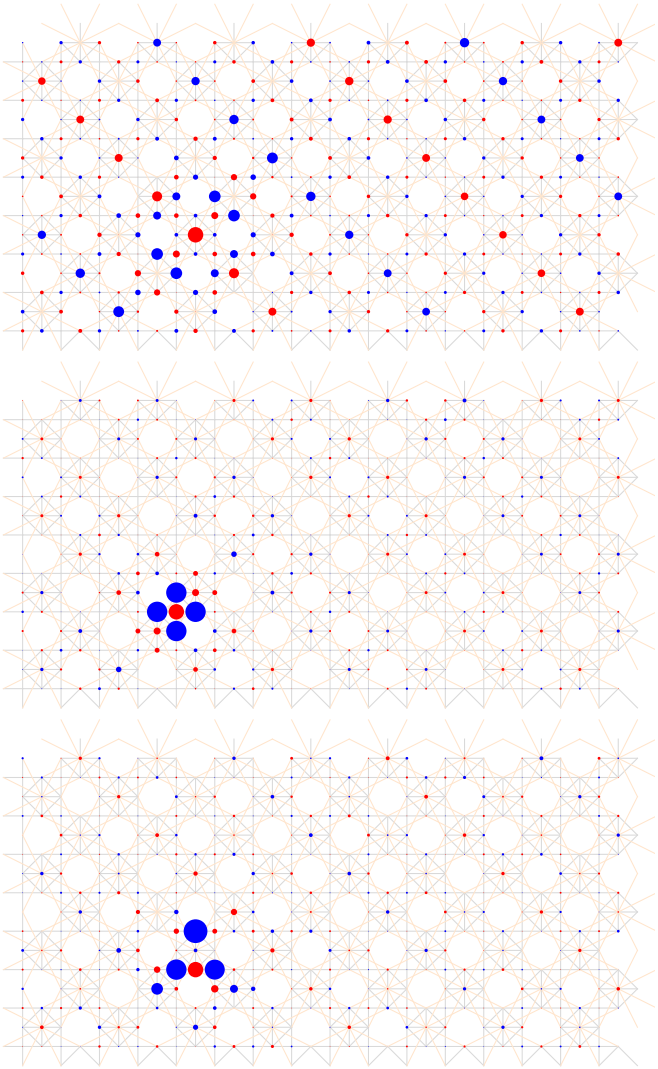

FIG. S11. Real space (equal-time) spin-spin correlations considering 3 reference sites: (top) Cu(3) spin, (middle) corner of triangles and (bottom) corner of square plaquette. The parameters are the ones extracted in the main text, $S \simeq 0.366$ here, for which the sum rule of the static structure factor is satisfied [S18]. The system size is $n_u \times 2 \times 6 \times 6$. The colors correspond to positive (blue) and negative (red) correlations. The reference site is always the largest red disk of the figure.


(2023), arXiv:2301.05224 [cond-mat.str-el].

[S7] T. Misawa, S. Morita, K. Yoshimi, M. Kawamura, Y. Motoyama, K. Ido, T. Ohgoe, M. Imada, and T. Kato, mVMC—Open-source software for many-variable variational Monte Carlo method, Comput. Phys. Commun **235**, 447 (2019).

[S8] D. Tahara and M. Imada, Variational Monte Carlo Method Combined with Quantum-Number Projection and Multi-Variable Optimization, J. Phys. Soc. Jpn. **77**, 114701 (2008).

[S9] S. Sorella, Green Function Monte Carlo with Stochastic Reconfiguration, Phys. Rev. Lett. **80**, 4558 (1998).

[S10] F. Becca and S. Sorella, *Quantum Monte Carlo Approaches for Correlated Systems* (Cambridge University Press, Cambridge, United Kingdom, 2017).

[S11] G. Carleo and M. Troyer, Solving the quantum many-body problem with artificial neural networks, Science **355**, 602 (2017).

[S12] N. Niggemann, B. Sbierski, and J. Reuther, Frustrated quantum spins at finite temperature: Pseudo-Majorana functional renormalization group approach, Phys. Rev. B **103**, 104431 (2021).

[S13] N. Niggemann, J. Reuther, and B. Sbierski, Quantitative functional renormalization for three-dimensional quantum Heisenberg models, SciPost Phys. **12**, 156 (2022).

[S14] A. Auerbach, *Interacting electrons and quantum magnetism* (Springer Science & Business Media, 1998).

[S15] J. C. Halimeh and M. Punk, Spin structure factors of chiral quantum spin liquids on the kagome lattice, Phys. Rev. B **94**, 104413 (2016).

[S16] R. Schaffer, Y. Huh, K. Hwang, and Y. B. Kim, Quantum spin liquid in a breathing kagome lattice, Phys. Rev. B **95**, 054410 (2017).

[S17] T. Lugan, L. D. C. Jaubert, and A. Ralko, Topological nematic spin liquid on the square kagome lattice, Phys. Rev. Res. **1**, 033147 (2019).

[S18] T. Lugan, L. D. C. Jaubert, M. Udagawa, and A. Ralko, Schwinger boson theory of the $J_1, J_2 = J_3$ kagome antiferromagnet, Phys. Rev. B **106**, L140404 (2022).